



OPEN Development of respiratory motion-resolved hepatobiliary phase cine-magnetic resonance imaging for stereotactic body radiotherapy in liver tumor

Ryuji Shimada^{1,2}, Keitaro Sofue¹✉, Tianyuan Wang³, Takeaki Ishihara³, Eisuke Ueshima¹, Yoshiko Ueno¹, Akiko Kusaka² & Takamichi Murakami¹

Cine-magnetic resonance imaging (MRI) has been used to track respiratory-induced motion of the liver and tumor and assist in the accurate delineation of tumor volume. Recent developments in compressed sensitivity encoding (SENSE; CS) have accelerated temporal resolution while maintaining contrast resolution. This study aimed to develop and assess hepatobiliary phase (HBP) cine-MRI scans using CS. Phantom was imaged using cine-MRI and signal intensity (SI) and contrast ratio (CR) measured to determine the optimal flip-angle turbo field echo (TFE) prepulse delay. We performed cine-MRI in 20 patients for one minute, with images taken every 0.5 s after administration of gadoxetic acid contrast agent. Acquired images had three different acceleration factors (SENSE, CS without denoising [CS-no], and CS with strong denoising [CS-strong]). The image quality of the HBP cine MRI was quantitatively and qualitatively analyzed. In the phantom study, a flip angle of 30 ° and TFE prepulse delay of 150 ms were optimal for clinical imaging. In a clinical study, CS-strong showed the highest signal-to-noise ratio and comparable contrast ratio among the three sequences. The CS-strong group showed a significantly higher image quality ($P < 0.01$), except for motion smoothness ($P = 0.11$). CS with denoising improved the tumor-to-liver contrast and image quality in high-temporal-resolution HBP cine MRI.

Cine images are used to evaluate movement. Cine magnetic resonance imaging (MRI) of the abdomen is also used in various situations¹, such as to track respiratory-induced motion of the liver and tumor in radiation therapy, assist accurate delineation of tumor volume, apply MRI-linac and cryotherapy^{2,3}, and in MRI-guided focused ultrasound surgery for treatment planning and real-time monitoring of the degree of heating. For radiotherapy of liver tumors, four-dimensional computed tomography (4D-CT) has been used as a cine image to evaluate the movement and delineate the liver and tumor^{4,5}. However, CT has several drawbacks, such as radiation exposure, occurrence of motion artifacts near the diaphragm owing to the ability to only obtain transverse images, and undetected tumors with non-contrast enhancement images⁶. Recently, respiratory motion-resolved cine MRI has been used to assess the motions of the liver and tumors in radiation planning⁷⁻⁹. However, liver tumors frequently cannot be visualized using balanced steady-state free precession (SSFP) and single-shot T2-weighted sequences because of poor tumor-to-liver contrast, although these have high temporal resolution¹⁰.

Gadoxetic acid-enhanced MRI improves the contrast between normal liver tissue and focal liver lesions¹¹; however, it is difficult to acquire cine-MRI with high temporal resolution. Recent developments in compressed sensing have accelerated scanning while maintaining a high temporal and contrast resolution^{12,13}. A method for acquiring cine-MRI while maintaining the contrast of hepatobiliary phase (HBP) images in gadoxetic acid-enhanced MRI has not been investigated. Thus, we developed a motion-resolved HBP cine-MRI. In these images, compressed SENSE (CS)-accelerated image acquisition using the reconstruction of sparse images from highly undersampled data was implemented¹⁴. We hypothesized that HBP cine MRI could be applied for radiotherapy planning for liver tumors when used in routine clinical practice. HBP cine MRI can provide accurate spatial and dynamic information on the abdominal organs, contributing to the intricate and comprehensive evaluation of

¹Department of Radiology, Kobe University Graduate School of Medicine, Kobe, Japan. ²Center for Radiology and Radiation Oncology, Kobe University Hospital, Kobe, Japan. ³Department of Radiation Oncology, Kobe University Graduate School of Medicine, Kobe, Japan. ✉email: keitarosofue@gmail.com

the liver and focal liver lesions. This study aimed to develop and assess HBP cine MRI with CS using phantoms and clinical cases.

Result

Phantom study

The signal intensity (SI) and contrast ratio (CR) results are shown in Fig. 1. The SI was larger when the FA was increased, and the turbo field echo (TFE) prepulse delay was lengthened. The CR increased slightly with FA between 20° and 30°, whereas it reached a peak value when an FA of 30° was applied for models with a higher CR. Overall, there was little change in FA for the models with the lowest CR. There was a tendency for the CR to improve as the TFE prepulse delay decreased in phantoms 1 and 2, but the overall CR was lower in phantom 3. A section of the acquired phantom image is shown in Fig. 2. As the FA increased, the TFEs were delayed and blur increased. For the assessment of the SI, increased FA and lengthened TFE prepulse achieved higher SI values. The CR increased slightly as the TFE prepulse lengthened, reaching a peak value when the FA was set at 30°. On the other hand, the TFE prepulse needed to be set to less than 200 ms to minimize blurring and maintain a sub-second temporal resolution. Consequently, we determined that an FA of 30° and a TFE prepulse delay of 150 ms were optimal for clinical imaging based on the evaluation of SI, CR, and blurring of the acquired phantom images.

Clinical study

The results of the signal-to-noise ratio (SNR) and CR in the clinical study are shown in Fig. 3. For the quantitative analysis, the SNR of liver (SNR_{Liv}) and tumor (SNR_{Tum}) were 6.8 ± 2.7 and 2.8 ± 0.8 for SENSE, 6.7 ± 2.8 and 3.0 ± 1.0 for CS without denoising (CS-no), and 14.4 ± 3.9 and 5.7 ± 2.8 for CS with strong denoising (CS-strong), respectively ($P < 0.001$). Cine-MRI with CS-strong demonstrated the highest SNR_{Liv} and SNR_{Tum} with significant differences compared with cine-MRI with SENSE and cine-MRI with CS-no. On the other hand, the $\text{CR}_{\text{Liv/Tum}}$ was 0.47 ± 0.13 for cine-MRI with SENSE, 0.43 ± 0.12 for cine-MRI with CS-no, and 0.49 ± 0.16 for cine-MRI with CS-strong ($P > 0.05$). CS was able to acquire images without changing the image contrast of HBP cine MRI. Table 1 presents the results of qualitative analyses. Qualitative analysis revealed significantly higher quality images of cine-MRI with CS-strong with regards to lesion conspicuity, contrast enhancement, image noise, and overall image quality ($P < 0.01$) than those of cine-MRI with SENSE and cine-MRI with CS-no (Fig. 4). Notably, CS had no negative impact on motion smoothness in the visual assessment ($P = 0.11$). The original cine-MR images of the three different imaging sequences are available as supplemental files.

Discussion

In the present study, we developed a motion-resolved HBP cine MRI using compressed SENSE, an accelerated image acquisition method that reconstructs sparse images from highly undersampled data. To validate the developed sequence, a phantom study was conducted to determine the optimal imaging parameters and a clinical study was performed to evaluate the highest image quality of the developed HBP cine MRI in patients with focal liver lesions. Our results suggest that the proposed HBP cine MRI using compressed SENSE is feasible for accurately assessing liver movements while achieving a high tumor-to-liver contrast-to-noise ratio. To the best of our knowledge, this is the first study to introduce an acceleration technique of compressed sensing into HBP cine-MRI scans. This sequence was shown to reduce acquisition time while maintaining image contrast and improving image quality, which has been impossible for clinical use because of significant image noise and artifacts.

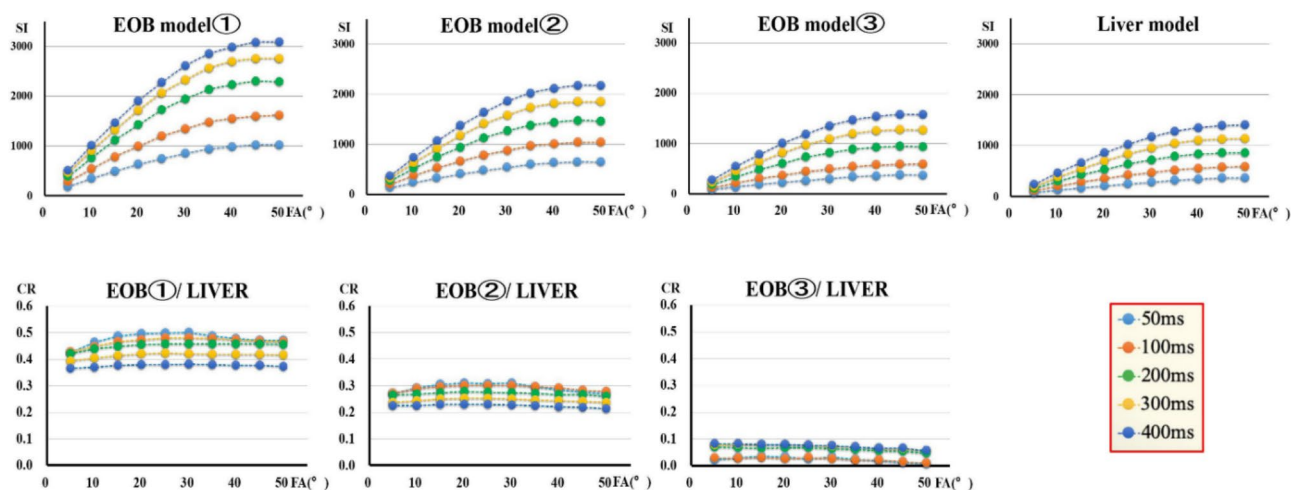


Fig. 1. The SI and CR results in the phantom study. The SI was larger when the FA was increased, and the TFE prepulse delay was lengthened. The CR increased slightly with FA between 20° and 30°. There was little change in FA for the models with the lowest CR. There was a tendency for the CR to improve as the TFE prepulse delay decreased in phantoms 1 and 2. SI, signal intensity; CR, contrast ratio; FA, flip angle; TFE, turbo field echo.

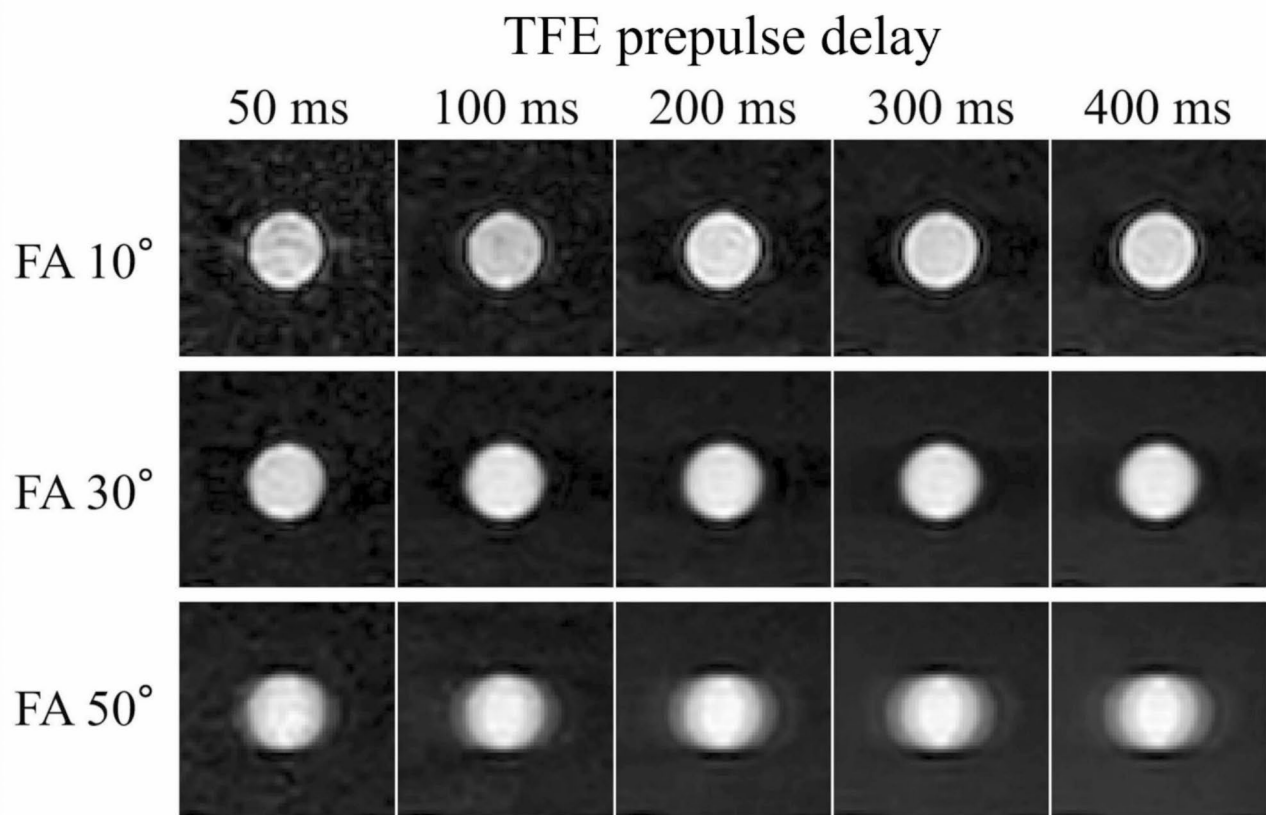


Fig. 2. Representative cine-magnetic resonance imaging phantom images with varying FA and TFE prepulse delay. The larger blurring occur as FA is increased or TFE prepulse delay lengthen. The signal-to-noise ratio and blurring are in the relationship of trade-off. FA, flip angle; TFE, turbo field echo.

In a phantom study, SI increased with an increase in FA, which concurs with previous clinical investigation^{15,16}. A TFE pre-pulse was used to suppress the background tissue and enhance the target object. However, as the TFE pre-pulse increased, blurring was strongly observed in the images as a tradeoff. The decrease in CR and increase in blurring artifacts with prolonged TFE prepulse delay are believed to be due to the reduced saturation effect and detection of slower tissue movement due to the prolonged data acquisition time¹⁷. CR is highly dependent on contrast uptake, with the lowest uptake model indicating that contrast enhancement is difficult to achieve, even with an FA or TFE prepulse delay. In clinical case selection, the uptake of the contrast agent in the liver parenchyma should be considered, as the gadoteric acid contrast agent is taken up by hepatocytes according to the functional reserve of the liver^{18–20}.

In our clinical study, no significant differences in SNRs were observed between cine-MRI with SENSE and cine-MRI with CS-no. This may be due to the fact that only the undersampling algorithm of the k-space trajectory is different and only the noise distribution is unidentical depending on the image reconstruction algorithm²¹. In contrast, SNRs of cine-MRI with CS-strong were twice as high as those of cine-MRI with SENSE and CS-no. The denoising process implemented using the compressed sensing algorithm might have contributed to this result²¹. In this study, there were no significant differences among the three different cine-MRI regarding CR. These results indicate that CS does not affect the signal intensity or image contrast in this sequence, even when a high temporal resolution is applied. Although there were no differences in CRs among the three images, significant improvements in qualitative image analysis were found for cine-MRI with CS-strong with respect to lesion conspicuity, contrast enhancement, and image noise. This may be due to the significant reduction in image noise provided by the CS. In addition, the denoising algorithm did not affect motion smoothness, indicating that noise may not have a significant influence on motion evaluation. CS can also suppress aliasing artifacts based on the random undersampling of the k-space trajectory, thereby enabling the application of the wavelet denoising algorithm²². We believe that the denoising algorithm significantly increases the SNR and contributes to the improvement of the contrast ratio and image quality in HBP cine MRI. Additionally, the implementation of a 3D reconstruction and respiratory phase-sorting algorithm is expected to deal with irregular breathing patterns and better simulate real clinical practice^{23,24}.

This study has several clinical implications. Cine MRI can be used for radiotherapy of the liver, which may lead to more accurate treatment planning, especially stereotactic body radiotherapy, which provides exceptional local control, improves survival rates, and minimizes adverse effects^{25,26}. Our proposed cine-MRI technique can improve the accuracy of target margin setting and treatment planning, potentially increasing the effectiveness of therapy and reducing its side effects. Previous studies for cine-MRI technique have mainly used balanced SSFP

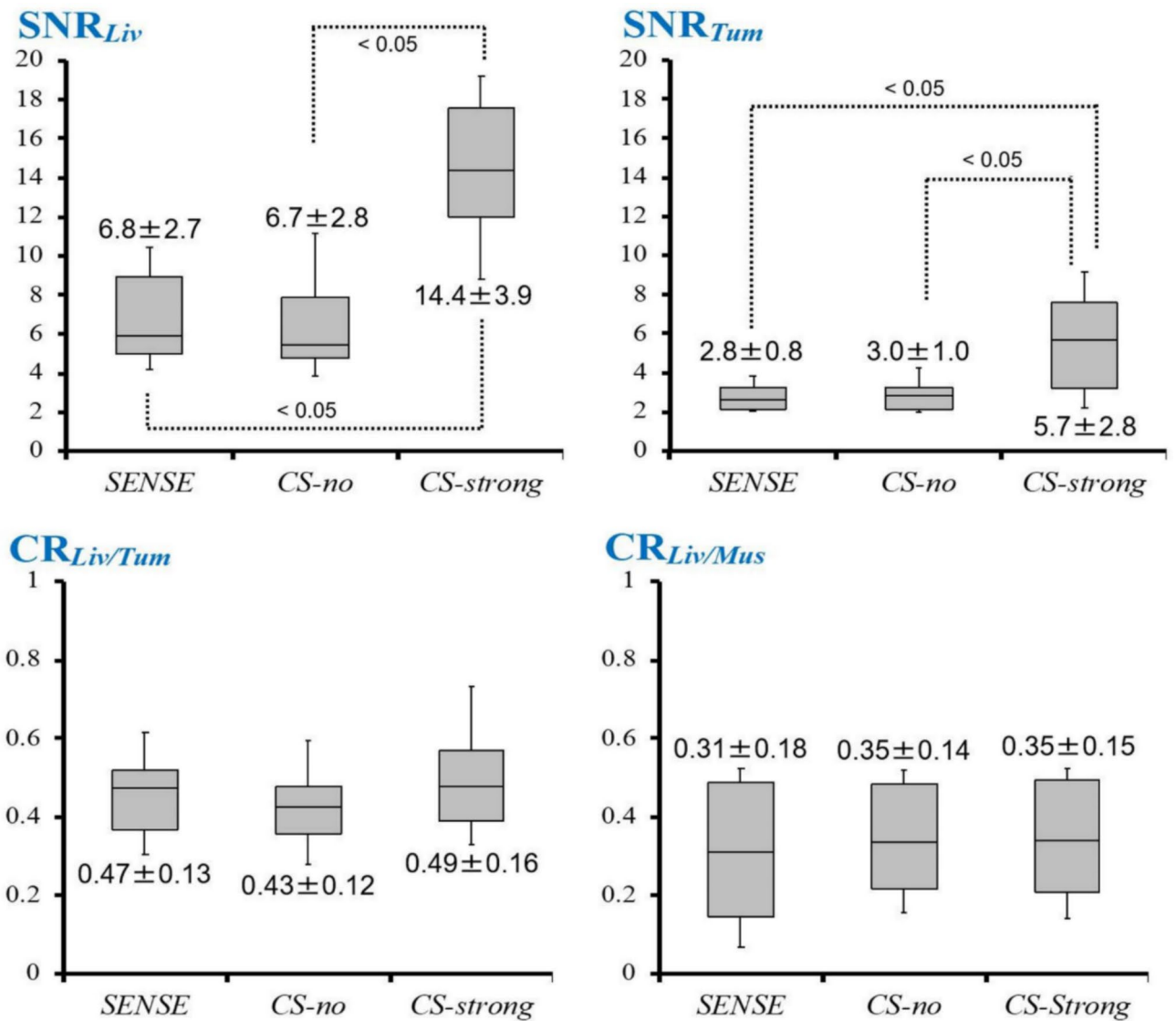


Fig. 3. Box plots of SNR and CR in the clinical study. Lower boundary of boxes indicates 25th percentile, line within boxes indicates median, and higher boundary of boxes indicates 75th percentile. Error bars indicate smallest and largest values within 1.5 box lengths of 25th and 75th percentiles. SNR_{Liv} = SNR of the liver, SNR_{Tum} = SNR of the tumor, CR_{Liv/Tum} = liver-to-tumor contrast ratio, CR_{Liv/Mus} = liver-to-muscle contrast ratio. SNR, signal-to-noise ratio; CR, contrast ratio; SENSE, sensitivity encoding; CS, compressed SENSE.

	SENSE	CS-no	CS-strong	P value
Lesion conspicuity	2.7 ± 1.1	2.8 ± 1.0	3.8 ± 0.4	< 0.01
Contrast enhancement	2.1 ± 1.0	2.2 ± 0.8	3.3 ± 0.8	< 0.01
Image noise	1.5 ± 0.6	1.5 ± 0.5	3.1 ± 0.7	< 0.01
Motion smoothness	2.9 ± 0.6	3.2 ± 0.5	3.3 ± 0.5	0.11
Overall image quality	1.9 ± 0.7	2.0 ± 0.7	3.3 ± 0.7	< 0.01

Table 1. Qualitative analysis in the clinical study. NOTE-. Measurement data are presented as mean ± standard deviation. SENSE, sensitivity encoding; CS, compressed SENSE; CS-no, CS-strong

or single-shot T2-weighted sequences^{9,27–29}. These sequences have the advantage of easily acquiring cine-MRI in other fields^{1,30}; however, they cannot clearly define the boundaries between the tumor and background liver tissue^{10,11}. In contrast, T1-weighted imaging is one of the basic sequences in liver MRI and is used for HBP images acquired approximately 20 min after the injection of a gadoteric acid contrast agent^{10,11}. To address the

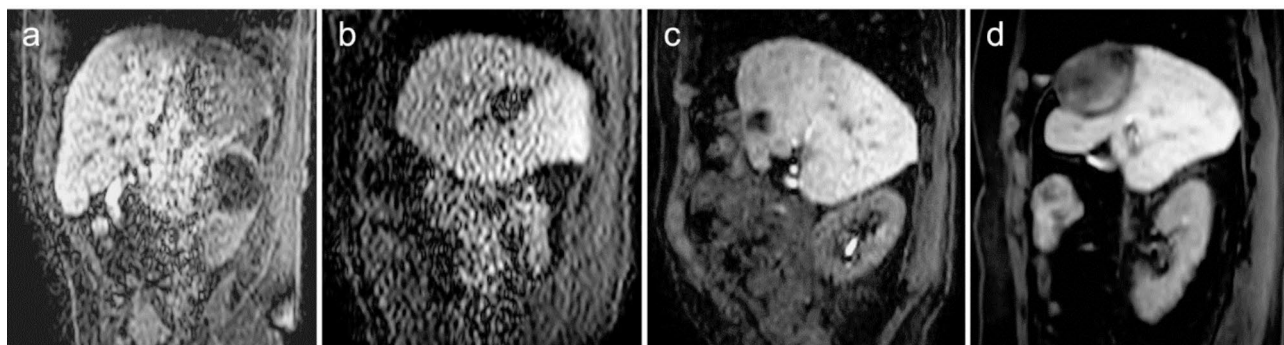


Fig. 4. Example of clinical cine-MRI with various visual scores. (a) cine-MRI with SENSE shows poor lesion conspicuity, excellent contrast enhancement, non-diagnostic image noise, good motion smoothness, and poor overall image quality. (b) cine-MRI with CS-no shows good lesion conspicuity, poor contrast enhancement, poor image noise, poor motion smoothness, and poor overall image quality. (c) cine-MRI with CS-strong shows good lesion conspicuity, good contrast enhancement, good image noise, excellent motion smoothness, and excellent overall image quality. (d) cine-MRI with CS-strong shows excellent lesion conspicuity, excellent contrast enhancement, excellent image noise, excellent motion smoothness, and excellent overall image quality.

	Previous paper ^{29–31}	Present cine-MRI
Applied sequence	Balanced SSFP Single-shot T2-weighted	Fat-suppressed T1-weighted after injection of gadoteric acid
Signal-to-noise ratio	Easy to secure	Difficult to secure
Tissue contrast	Good tissue contrast	Good tissue contrast
Detection of focal liver lesion	Difficult to detect	Easy to detect
Related image artifacts	Banding artifact Severe blurring	Faint blurring

Table 2. Comparison of cine-magnetic resonance imaging (MRI) sequence between our work and previous paper.

poor soft-tissue contrast in balanced SSFP or single-shot T2-weighted sequences for moving target detection of focal liver lesions as well as the challenges of achieving sufficient temporal-spatial resolution, we developed an HBP cine MRI that achieves high temporal-spatial resolution while maintaining optimal tumor-to-liver contrast (Table 2). Additionally, patients with hepatocellular carcinoma have a history of chronic liver disease, which poses a potential risk for liver decompensation following stereotactic body radiotherapy (SBRT). Recent proposals suggest individualized adaptive SBRT using the indocyanine green retention test as an estimate of the functional liver reserve³¹.

Our study has some limitations. First, this was a single-center, retrospective study with a relatively small number of patients. However, significant differences were observed in most analyses and similar results will be expected from studies with larger numbers of patients. Second, comparisons between our developed HBP cine-MRI with CS and other cine-MRI sequences were not performed. Further studies are needed to determine whether the HBP cine MRI sequence can be used instead of other sequences. Third, this study did not perform specific measures to account for potential confounding factor in the clinical study. Consequently, the target population included various types of liver tumors with different ages and genders. Forth, we did not evaluate the clinical utility of the proposed method for detecting and delineating focal liver lesions for stereotactic body radiotherapy planning, which warrants further clinical investigation. Finally, a single-vendor MRI scanner was used. Future studies using other MRI scanners with different CS algorithms are required to determine whether the results can be replicated using other MRI scanners.

In conclusion, the developed sequence of HBP cine-MRI using compressed SENSE with denoising improved the tumor-to-liver visual contrast and image quality. For radiotherapy in the liver, our proposed method may lead to more precise treatment planning by allowing the accurate assessment of both lesion boundaries and respiratory-correlated motions. Future studies including large number of patients are required to focus on validating and demonstrating utility of HBP cine-MRI for more accurate radiotherapy treatment planning.

Methods

Phantom study

Phantom preparation

Four phantoms of gadoteric acid contrast agent diluted in saline were created and adjusted to different T1 values. A commercial MRI phantom (Model 90-401 enclosed phantom, NikkoFines, Japan), which measures 220 mm in diameter and 130 mm in length, was employed to conduct the evaluation systematically. Four cylindrical

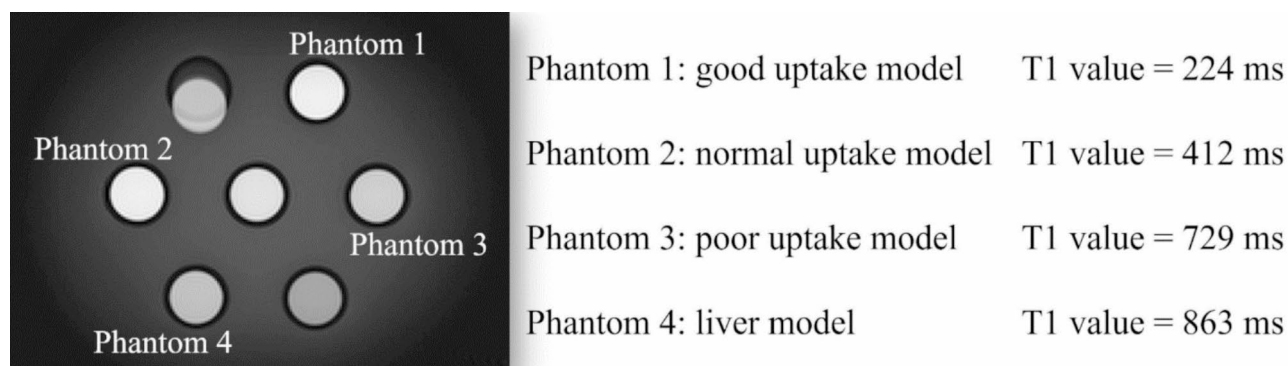


Fig. 5. Example of for the phantom model. Four phantoms of gadoxetic acid contrast agent diluted in saline were created and adjusted to different T1 values.

Sequence	Phantom study	Clinical study
Acquisition mode	Cartesian	Cartesian
Shot mode	Single-shot	Single-shot
Freq FOV (cm) / phase FOV	256×256	380×300
Slice thickness / spacing (mm)	1 / 0	3 / 0
Number of slice	1	2
Cross sectional image	Coronal	Sagittal
Voxel size (reconstructed)	1.0×1.0×1.0	1.0×1.0×3.0
TR (ms)	2.7	3.1
TE (ms)	1.23	1.46
Flip angle (degree)	5/10/15/20/25/30/35/40/45/50	30
Bandwidth (Hz)	868.1	1083.5
Fat suppression	SPIR	SPIR
TFE factor	32	40
Shot interval	Shortest	Shortest
TFE prepulse / pulse type	Saturate/Composite	Saturate / Composite
TFE prepulse delay (ms)	50/100/200/300/400	150
TFE shot duration (ms)	246.8	285
Accelerated factor	CS 4	SENSE 4 / CS 4
Denoising level	Strong	No / Strong

Table 3. MRI Acquisition parameters in Phantom and Clinical Study. FOV, field of view; TR, repetition time; TE, echo time; TFE, turbo field echo; SPIR, spectral presaturation with inversion recovery; SENSE, sensitivity encoding; CS, compressed SENSE.

crystal carboy bottles 30 mm in diameter were prepared. In these bottles, several concentrations of solution (T1 values: phantom 1, 224 ms/ good uptake model; phantom 2, 412 ms/normal uptake model; phantom 3, 729 ms/ poor uptake model; phantom 4, 863 ms/liver model; Fig. 5) were enclosed to estimate the different amount of gadoxetic acid uptake. These bottles were then inserted into the commercial MRI phantom for the acquisition of the MR images. T1 values were selected based on several clinical data in previous papers³² and measured using the inversion recovery method.

MR imaging technique in the phantom study

The phantoms were imaged using 3.0T MRI scanner (Ingenia3.0T version5.4, Philips Medical Systems, Netherlands) under different imaging conditions. Model 90-401enclosed phantom (NikkoFines, Japan) was imaged using a torso 32 channel coil (anterior 16 channels + posterior 16 channels), which was used to image the abdomen. The imaging parameters are listed in Table 3, and the sequence schema is shown in Fig. 6. In this phantom study, MRI was performed without SENSE, because we emphasize on determining optimal imaging parameters.

A sequence of 2D-T1- TFE (K-space order: low-high) with spectral pre-saturation with inversion recovery (SPIR) and a saturation pulse was used, and images were acquired at the same slice position, assuming free breathing. Images were acquired while varying the FA (5°-50° degree, 10 steps) and TFE prepulse delay (50, 100, 200, 300, 400 ms), and the one-shot duration was set to less than 0.5–1.0 s. Consequently, a total of 50

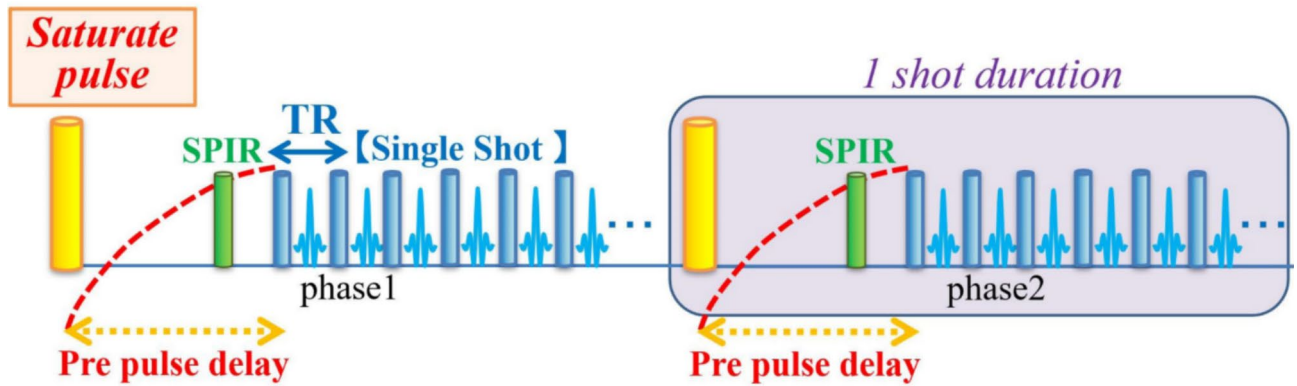


Fig. 6. Acquisition schema of cine-magnetic resonance imaging sequence in the phantom study. Prepulse is applied to maintain image contrast to complement the phenomenon that continuous signal acquisitions cause signal degradation due to insufficient recovery of longitudinal magnetization. TR repetition time; SPIR, spectral presaturation with inversion recovery.

image datasets (ten types of FA \times five TFE prepulse delay = 50 datasets) were obtained for the analyses in this phantom study. The phantom was placed at the center of the magnetic field, and images were acquired 1 h later. Subsequently, the receiver gain was fixed for each scan.

Evaluation methods

SI and CR were measured to evaluate image quality with regard to image contrast and quality in the 50 image datasets. The SI was calculated as the average value of 10 consecutive images under each condition by placing oval regions of interest on each phantom (phantom 1–4). The regions of interest (ROIs) in each region were as large as possible. We used the following formula to calculate the CR for the subjective evaluation of image contrast between the uptake models (phantom 1–3) and liver models (phantom 4), assuming liver-to-lesion contrast, as used in previous papers^{32,33}.

$$CR = (SI_{\text{Uptake model}} - SI_{\text{Liver model}}) / (SI_{\text{Uptake model}} + SI_{\text{Liver model}})$$

Clinical study

Study design

This study was a retrospective analysis of prospectively collected data from a single center and was approved by the institutional review board of Kobe University (approval no. 197270). The requirement for written informed consent was waived from the ethics committee of Kobe University Hospital because of the retrospective nature of the study. In this study, all procedures were conducted in accordance with the ethical standards of our institution and the National Research Committee, as well as with the Declaration of Helsinki.

Twenty patients (men: women = 13:7, 39–84 years) who underwent gadoteric acid-enhanced MRI with at least one focal liver lesion between February 2019 and April 2019 were included in the study to develop and assess HBP cine-MRI clinically using CS. The HBP cine-MRI was performed as a part of routine clinical practice in liver MR imaging protocol. The patients had hepatocellular carcinoma ($n=9$), colorectal liver metastasis ($n=5$), hemangioma ($n=4$), or cholangiocarcinoma ($n=2$). Nine patients had normal liver function with no history of chronic liver disease, whereas eleven had chronic liver function: hepatitis C virus ($n=5$), alcoholic chronic hepatitis ($n=2$), hepatitis B virus ($n=1$), and cryptogenic disease ($n=3$). In patients with chronic liver disease, nine and two patients were classified as Child-Pugh A and B. We compared three acceleration techniques to identify the differences between SENSE and CS. “SENSE” indicates sequence with SENSE accelerate factor 4, “CS-no” CS factor 4 without denoising, and “CS-strong” CS factor 4 with strong denoising level.

MR imaging technique in the clinical study

The patients underwent MRI using 3.0T MRI scanner (Ingenia3.0T ver5.4, Philips Medical Systems, Netherlands) under three different imaging conditions. All images were acquired using a torso 32 channel coil (16 channel anterior + 16 channel posterior), which is commonly used for normal abdominal imaging. A sequence of 2D-T1-TFE (K-space order: low-high) with SPIR and a saturated pulse was used similar to the phantom scan. Imaging parameter of cine-MRI was set at FA of 30° and TFE prepulse delay of 150 ms based on the aforementioned phantom study to maintain signal intensity and temporal resolution, and images were acquired every 0.57 s (0.285 \times 2 slice) under free breathing. The imaging parameters are listed in Table 3, and the sequence schema is shown in Fig. 7. Three imaging conditions were used to achieve the same acquisition time.

Quantitative analysis

The SI of the tumor, normal liver, and paraspinal muscle were measured by placing regions of interest from 10 consecutive cine images. The SI value of each tumor was positioned as large as possible, and the SI value of the liver parenchyma was measured in the average of the three 100-mm² circular ROIs adjacent to the tumor. The

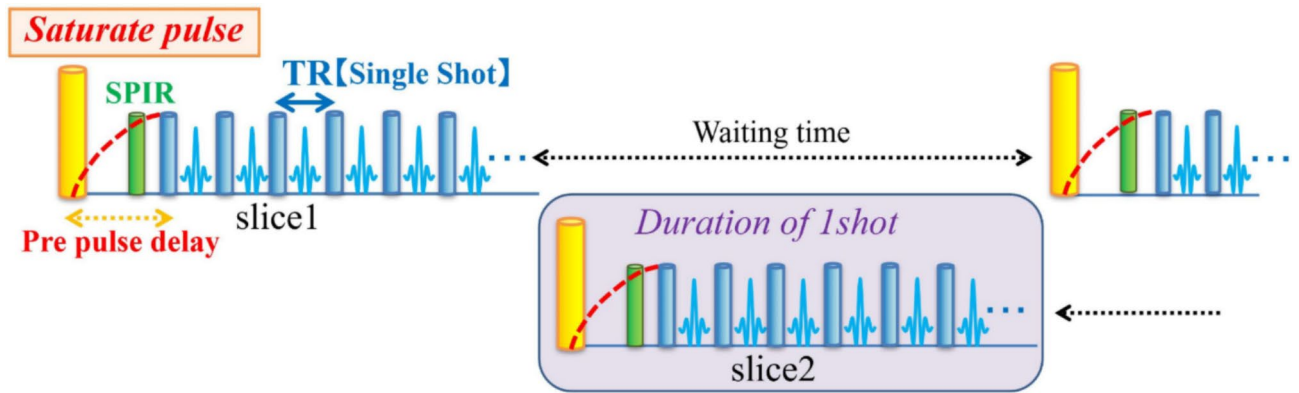


Fig. 7. Acquisition schema of cine-magnetic resonance imaging sequence in the clinical study. The sequence is designed to accelerate the recovery of longitudinal magnetization and maintain signal to noise ratio by acquiring two slice images simultaneously and creating a waiting time for each slice without changing the shot interval. TR, repetition time; SPIR, spectral presaturation with inversion recovery.



Fig. 8. Representative cine-magnetic resonance imaging images with SENSE, CS-no, and CS-strong. Image artifact caused by parallel imaging is evident in the center of the image with SENSE. Mild image artifact is distributed through the whole range of the image with CS-no, whereas the artifact is reduced in the image with CS-strong. SENSE, sensitivity encoding; CS, compressed SENSE.

signal-to-noise ratio of the liver and tumor (SNR_{Liv} , SNR_{Tum}) and the liver-to-tumor and liver-to-muscle contrast ratios ($CR_{Liv/Tum}$, $CR_{Liv/Mus}$) were calculated using the following formula^{33,34}. The mean SNR and CR of the 20 patients were calculated under these three conditions.

$$SNR = Sp/Np$$

$$CR = (Sp_1 - Sp_2) / (Sp_1 + Sp_2)$$

Sp: signal intensity of each ROI, Np: standard deviation of each ROI, Sp_1 : signal intensity of ROI₁, Sp_2 : signal intensity of ROI₂.

Qualitative analysis

For qualitative analysis, lesion conspicuity, contrast enhancement, image noise, motion smoothness, and overall image quality were evaluated and scored by two radiologists (16 and 21 years of experience) on a 4-point scale (excellent, 4; good, 3; poor, 2; non-diagnosis, 1) in consensus under the three conditions (Fig. 8).

Statistical analysis

Continuous variables are expressed as mean \pm standard deviation. The Shapiro–Wilk test was used to confirm the normality of the data distribution. The calculated SNR and CR were compared among the three conditions using repeated-measures analysis of variance, and post-hoc pairwise comparisons were performed using the Student–Neuman–Keulstest for statistically significant parameters. The Kruskal–Wallis H-test was used for qualitative analysis. Power calculations were performed to estimate the necessary sample size to detect a difference in SNR_{Liv} and SNR_{Tum} in each patient calculated from images with SENSE, CS-no, and CS strong. These were based on a two-sided test with significance level $\alpha=0.05$, and a power of 80%. It was assumed that the means were

normally distributed and the variances of the two groups were the same. The power calculation revealed that a 10% difference can be observed with 15 and 18 subjects in SNR_{Liv} and SNR_{Tum} , respectively.

All statistical analyses were performed using commercially available software (SPSS version 20.0, IBM, Chicago, IL). P values were considered statistically significant at $P < 0.05$.

Data availability

The datasets used and/or analyzed during the current study are available from the corresponding author on reasonable request.

Received: 1 December 2023; Accepted: 9 December 2024

Published online: 28 December 2024

References

1. Ueki, H. et al. Efficacy of preoperative cine magnetic resonance imaging in evaluation of adhesion of renal cancer thrombus to inferior vena cava wall. *J. Vasc. Surg. Venous Lymphat. Disord.* **10**, 908–915 (2022).
2. Wijlemans, J. W. et al. A clinically feasible treatment protocol for magnetic resonance-guided high-intensity focused ultrasound ablation in the liver. *Invest. Radiol.* **50**, 24–31 (2015).
3. Placidi, L. et al. Quantitative analysis of MRI-guided radiotherapy treatment process time for tumor real-time gating efficiency. *J. Appl. Clin. Med. Phys.* **21**, 70–79 (2020).
4. Xi, M. et al. Defining internal target volume (ITV) for hepatocellular carcinoma using four-dimensional CT. *Radiother. Oncol.* **84**, 272–278 (2007).
5. Tascón-Vidarte, J. D. et al. Accuracy and consistency of intensity-based deformable image registration in 4DCT for tumor motion estimation in liver radiotherapy planning. *PLoS One* **17**, e0271064 (2022).
6. Keall, P. J. et al. The management of respiratory motion in radiation oncology report of AAPM Task Group 76. *Med. Phys.* **33**, 3874–3900 (2006).
7. Stemkens, B., Paulson, E. S. & Tijssen, R. H. N. Nuts and bolts of 4D-MRI for radiotherapy. *Phys. Med. Biol.* **63**, 21TR01 (2018).
8. Mickevicius, N. J. & Paulson, E. S. Investigation of undersampling and reconstruction algorithm dependence on respiratory correlated 4D-MRI for online MR-guided radiation therapy. *Phys. Med. Biol.* **62**, 2910–2921 (2017).
9. Freedman, J. N. et al. T2-Weighted 4D magnetic resonance imaging for application in magnetic resonance-guided radiotherapy treatment planning. *Invest. Radiol.* **52**, 563–573 (2017).
10. Van den Bos, I. C. et al. MR imaging of hepatocellular carcinoma: Relationship between lesion size and imaging findings, including signal intensity and dynamic enhancement patterns. *J. Magn. Reson. Imaging* **26**, 1548–1555 (2007).
11. Murakami, T., Sofue, K. & Hori, M. Diagnosis of hepatocellular carcinoma using Gd-EOB-DTPA MR imaging. *Magn. Reson. Med. Sci.* **21**, 168–181 (2022).
12. Jaspan, O. N., Fleysler, R. & Lipton, M. L. Compressed sensing MRI: A review of the clinical literature. *Br. J. Radiol.* **88**, 20150487 (2015).
13. Wu, C. et al. 4D lung MRI with high-isotropic-resolution using half-spoke (UTE) and full-spoke 3D radial acquisition and temporal compressed sensing reconstruction. *Phys. Med. Biol.* <https://doi.org/10.1088/1361-6560/acace6> (2023).
14. Kocaoglu, M. et al. Breath-hold and free-breathing quantitative assessment of biventricular volume and function using compressed SENSE: A clinical validation in children and young adults. *J. Cardiovasc. Magn. Reson.* **22**, 54 (2020).
15. Haimerl, M. et al. Gd-EOB-DTPA-enhanced MRI for evaluation of liver function: Comparison between signal-intensity-based indices and T1 relaxometry. *Sci. Rep.* **7**, 43347 (2017).
16. Rosenkrantz, A. B. et al. Breath-hold T2-weighted MRI of the liver at 3T using the BLADE technique: Impact upon image quality and lesion detection. *Clin. Radiol.* **66**, 426–433 (2011).
17. Shanbhogue, K. et al. Accelerated single-shot T2-weighted fat-suppressed (FS) MRI of the liver with deep learning-based image reconstruction: Qualitative and quantitative comparison of image quality with conventional T2-weighted FS sequence. *Eur. Radiol.* **31**, 8447–8457 (2021).
18. Haradome, H. et al. Gadoteric acid disodium-enhanced hepatocyte phase MRI: Can increasing the flip angle improve focal liver lesion detection?. *J. Magn. Reson. Imaging* **35**, 132–139 (2012).
19. Bashir, M. R. et al. Liver MRI in the hepatocyte phase with gadolinium-EOB-DTPA: Does increasing the flip angle improve conspicuity and detection rate of hypointense lesions?. *J. Magn. Reson. Imaging* **35**, 611–616 (2012).
20. Wheaton, A. J. & Miyazaki, M. Non-contrast enhanced MR angiography: Physical principles. *J. Magn. Reson. Imaging* **36**, 286–304 (2012).
21. Motosugi, U. et al. Liver parenchymal enhancement of hepatocyte-phase images in Gd-EOB-DTPA-enhanced MR imaging: Which biological markers of the liver function affect the enhancement?. *J. Magn. Reson. Imaging* **30**, 1042–1046 (2009).
22. Okada, M. et al. Biochemical and clinical predictive approach and time point analysis of hepatobiliary phase liver enhancement on Gd-EOB-DTPA-enhanced MR images: A multicenter study. *Radiology* **281**, 474–483 (2016).
23. Tsujita, Y. et al. Prediction of post-hepatectomy liver failure using gadoteric acid-enhanced magnetic resonance imaging for hepatocellular carcinoma with portal vein invasion. *Eur. J. Radiol.* **130**, 109189 (2020).
24. Feng, L. et al. Compressed sensing for body MRI. *J. Magn. Reson. Imaging* **45**, 966–987 (2017).
25. Chen, C. & Huang, J. Exploiting the wavelet structure in compressed sensing MRI. *Magn. Reson. Imaging* **32**, 1377–1389 (2014).
26. Liu, Y. et al. Accuracy of respiratory motion measurement of 4D-MRI: A comparison between cine and sequential acquisition. *Med. Phys.* **43**, 179 (2016).
27. van de Lindt, T. et al. A self-sorting coronal 4D-MRI method for daily image guidance of liver lesions on an MR-LINAC. *Int. J. Radiat. Oncol. Biol. Phys.* **102**, 875–884 (2018).
28. Mahadevan, A. et al. Stereotactic Body Radiotherapy (SBRT) for liver metastasis—clinical outcomes from the international multi-institutional RSSearch® Patient Registry. *Radiat. Oncol.* **13**, 26 (2018).
29. Birgin, E. et al. Stereotactic body radiation therapy versus surgical resection for stage I/II hepatocellular carcinoma. *Cancers (Basel)* **15**, 2330 (2023).
30. Paganelli, C. et al. Liver 4DMRI: A retrospective image-based sorting method. *Med. Phys.* **42**, 4814–4821 (2015).
31. Harris, W. et al. Accelerating volumetric cine MRI (VC-MRI) using undersampling for real-time 3D target localization/tracking in radiation therapy: A feasibility study. *Phys. Med. Biol.* **63**, 01NT01 (2017).
32. Han, F. et al. Respiratory motion-resolved, self-gated 4D-MRI using Rotating Cartesian K-space (ROCK): Initial clinical experience on an MRI-guided radiotherapy system. *Radiother. Oncol.* **127**, 467–473 (2018).
33. Barten, D. L. J. et al. A 3D cine-MRI acquisition technique and image analysis framework to quantify bowel motion demonstrated in gynecological cancer patients. *Med. Phys.* **48**, 3109–3119 (2021).
34. Feng, M. et al. Individualized adaptive stereotactic body radiotherapy for liver tumors in patients at high risk for liver damage: A phase 2 clinical trial. *JAMA Oncol.* **4**, 40–47 (2018).

Author contributions

K.S. initiated the study and made substantial contributions to the conception and design of the study and data analysis. K.S., R.S., W.T., Y.U., and T.I. contributed substantially to data acquisition. R.S. wrote the manuscript. K. S., W. T., T. I., Y. U., E. U., A. K., and T. M. critically revised the manuscript for important intellectual content. All authors reviewed the manuscript and agree to be accountable for all aspects of this study.

Declarations

Competing interests

The authors declare no competing interests.

Additional information

Supplementary Information The online version contains supplementary material available at <https://doi.org/10.1038/s41598-024-82860-3>.

Correspondence and requests for materials should be addressed to K.S.

Reprints and permissions information is available at www.nature.com/reprints.

Publisher's note Springer Nature remains neutral with regard to jurisdictional claims in published maps and institutional affiliations.

Open Access This article is licensed under a Creative Commons Attribution-NonCommercial-NoDerivatives 4.0 International License, which permits any non-commercial use, sharing, distribution and reproduction in any medium or format, as long as you give appropriate credit to the original author(s) and the source, provide a link to the Creative Commons licence, and indicate if you modified the licensed material. You do not have permission under this licence to share adapted material derived from this article or parts of it. The images or other third party material in this article are included in the article's Creative Commons licence, unless indicated otherwise in a credit line to the material. If material is not included in the article's Creative Commons licence and your intended use is not permitted by statutory regulation or exceeds the permitted use, you will need to obtain permission directly from the copyright holder. To view a copy of this licence, visit <http://creativecommons.org/licenses/by-nc-nd/4.0/>.

© The Author(s) 2024